Asia-Pac. J. Atmos. Sci., 53(4), 519-536, 2017
DOI:10.1007/s13143-017-0055-y
pISSN 1976-7633 / eISSN 1976-7951

Evaluate Dry Deposition Velocity of the Nitrogen Oxides Using Noah-MP Physics Ensemble Simulations for the Dinghushan Forest, Southern China

Qi Zhang[1], Ming Chang[2], Shengzhen Zhou[1], Weihua Chen[3], Xuemei Wang[2], Wenhui Liao[2], Jianing Dai[3], and ZhiYong Wu[2]

[1]*School of Atmospheric Sciences, Sun Yat-sen University, Guangzhou, China*
[2]*Institute for Environmental and Climate Research, Jinan University, Guangzhou, China*
[3]*School of Environmental Science and Engineering, Sun Yat-sen University, Guangzhou,China*

(Manuscript received 27 October 2016; accepted 28 April 2017)

Abstract: There has been a rapid growth of reactive nitrogen (N_r) deposition over the world in the past decades. The Pearl River Delta region is one of the areas with high loading of nitrogen deposition. But there are still large uncertainties in the study of dry deposition because of its complex processes of physical chemistry and vegetation physiology. At present, the forest canopy parameterization scheme used in WRF-Chem model is a single-layer "big leaf" model, and the simulation of radiation transmission and energy balance in forest canopy is not detailed and accurate. Noah-MP land surface model (Noah-MP) is based on the Noah land surface model (Noah LSM) and has multiple parametric options to simulate the energy, momentum, and material interactions of the vegetation-soil-atmosphere system. Therefore, to investigate the improvement of the simulation results of WRF-Chem on the nitrogen deposition in forest area after coupled with Noah-MP model and to reduce the influence of meteorological simulation biases on the dry deposition velocity simulation, a dry deposition single-point model coupled by Noah-MP and the WRF-Chem dry deposition module (WDDM) was used to simulate the deposition velocity (V_d). The model was driven by the micro-meteorological observation of the Dinghushan Forest Ecosystem Location Station. And a series of numerical experiments were carried out to identify the key processes influencing the calculation of dry deposition velocity, and the effects of various surface physical and plant physiological processes on dry deposition were discussed. The model captured the observed V_d well, but still underestimated the V_d. The self-defect of Wesely scheme applied by WDDM, and the inaccuracy of built-in parameters in WDDM and input data for Noah-MP (e.g. LAI) were the key factors that cause the underestimation of V_d. Therefore, future work is needed to improve model mechanisms and parameterization.

Key words: Nitrogen deposition, dry deposition velocity, nitrogen oxides, Noah - MP, WRF - Chem

1. Introduction

Transportation and deposition of nitrogen-containing compounds are two of the most critical processes in biogeochemical cycling (Gruber and Galloway, 2008). Atmospheric nitrogen deposition is the main removal process of atmospheric reactive nitrogen (N_r) and the important nitrogen source for ecosystem. The rapid global economic development and population expansion have resulted in a remarkable increase in atmospheric N_r emissions. Anthropogenic nitrogen emissions have rose from 15 Tg N yr $^{-1}$ in 1860 to 156 TgN yr $^{-1}$ in 1995, and reached 207 TgN yr $^{-1}$ in 2008 (Galloway and Cowling, 2002; Canfield et al., 2010). Liu et al. (2013) constructed a national data set incorporating all the available bulk nitrogen deposition results from monitoring sites throughout China between 1980 and 2010, finding that the average nitrogen deposition flux has increased by 60% over China in this period. The increment of nitrogen deposition results in the exceedance of critical load and causes a significant impact on the structure and function of ecosystems at the global and regional scale (Stevens et al., 2004; Horii et al., 2006; Chen et al., 2012).

The major components of atmospheric N_r are NH_x and NO_y (Sharma et al., 2010). Nitrogen fertilizer related to agricultural activities is the principal source of NH_x, while motor vehicles and the combustion of fossil fuels are the main sources of NO_y (Vaittinen et al., 2014). The Pearl River Delta region (PRD), as one of the China's three biggest urban clusters, has undergone a substantial raise of N_r emissions (Ameur-Bouddabbous et al., 2012). NO_x ($NO + NO_2$), as the main component of N_r, is the important precursor of pollutants (e.g. fine particulates and O_3), which causes severe atmospheric pollution in the PRD (Chen et al., 2012; Han and Song, 2012; Shen et al., 2015; Tariq et al., 2016; Wang et al., 2016). Sun et al. (2014) found that the critical load of nitrogen deposition was lower than that of sulfur deposition in PRD, and the lowest value occurred in Zhaoqing area, indicating the ecological environment in the PRD is more sensitive to nitrogen deposition, especially in Zhaoqing area.

Atmospheric N_r is removed by wet and dry deposition process, and the accurate estimation of its deposition flux is an important basis for assessing its ecological effects. A series of researches have been done on the wet deposition of N_r (Lü and Tian, 2007; Pan et al., 2012; Du et al., 2014; Liu et al., 2015), but there are still large uncertainties in the study of dry deposition because of its complex processes of physical chemistry and vegetation physiology (Byun and Schere, 2006,

Corresponding Author: Xue-Mei Wang & Ming Chang, Institute for Environmental and Climate Research, Jinan University, No. 855, Xingye Avenue East, Panyu District, Guangzhou 510632, China.
E-mail: eeswxm@mail.sysu.edu.cn; changming@jnu.edu.cn

Petroff et al., 2008).

At present, the forest canopy parameterization scheme used in WRF-Chem model is a single-layer "big leaf" model, and the simulation of radiation transmission and energy balance in forest canopy is not detailed and accurate, especially in the forest area (Wesely and Hicks, 2000). Noah-MP land surface model (Noah-MP) is based on the Noah land surface model (Noah LSM) and has multiple parameterization options to simulate the energy, momentum, and material interactions of the vegetation-soil-atmosphere system. It inherits the advantages of Noah LSM that the process of hydrothermal coupling is comprehensive and widely used (Niu et al., 2011). On this basis, it constructs a canopy that can define the height, crown radius, density, radiation characteristics, etc. It introduces a double stream radiation transfer scheme which takes into account the effects of canopy shadow, rain and snow, internal hydrothermal transmission. It introduces a mechanism such as TOPography based hydrological MODEL(TOPMODEL) into the runoff and groundwater processes. A dynamic vegetation growth model is used to simulate the physiological processes of vegetation. The above processes are organically coupled to make up the over-simplified defects of Noah LSM in the simulation of vegetation, soil, hydrological and other interactions.

Therefore, to investigate the improvement of the simulation results of WRF-Chem on the nitrogen deposition in forest area after coupled with Noah-MP model and reduce the influence of meteorological simulation biases on the dry deposition velocity (V_d) simulation, a dry deposition single-point model coupled by Noah-MP and the WRF-Chem dry deposition module (WDDM) was used to simulate the V_d. The model was driven by the micro-meteorological observation of the Dinghushan Forest Ecosystem Research Station. And a series of numerical experiments were carried out to identify the key processes influencing the calculation of dry deposition velocity, and the effects of various surface physical and plant physiological processes on dry deposition were discussed. And the measurement of NO_x concentration gradient, dry deposition flux and micrometeorological data was carried out in the site in the same period with the lushest vegetation growth from 1 August to 30 September 2015, during which the NO_x concentration difference between canopy interior and canopy exterior is relatively larger due to more foliage of plants blocking the deposition of the gaseous substances. In addition, the Dinghushan Nature Reserve in Zhaoqing has a well-preserved southern subtropical monsoon evergreen broad-leaved forest community and diverse transitional vegetation, which are rare in the vicinity of the Tropic of Cancer. The higher primary productivity makes the Dinghushan forest have an important influence on the process of material circulation of the global ecosystem. It is important to carry out the observation and simulation of NO_x in the area. To understand the dry deposition characteristics of NO_x in Dinghushan area and nitrogen Biogeochemical cycle is of great significance.

2. Methodology

a. Observation site

Dinghushan National Nature Reserve is located in Dinghu District, Zhaoqing City, Guangdong Province, at the northwest edge of the PRD (112°30'39"E-112°33'41"E, 23°09'21"N-23°11'30"N). The region with an area of 1,150 hectares, is one of the few subtropical forest systems in the desert belt near the Tropic of Cancer (Tang et al., 2003). Most of the region belongs to hilly terrain and the climate is humid subtropical monsoon climate with an annual average sunshine duration of 1432.7 hours and a sunshine rate of 32.8% (Wang et al., 2007). The corresponding short-term observation of total solar radiation is 104.8-116.6 $kcal \cdot cm^{-1} \cdot yr^{-1}$ (Kong et al., 1996). The average annual temperature and rainfall is 20.1°C and 1927 mm, respectively, and obvious drought and rainy seasons are found in this region. Dinghushan has a vertical band spectrum from 14 m to 1,000 m above sea level. The red soils of latosol red are mainly distributed below 700 m and the yellow soil is primarily distributed 700 m above. In terms of vegetation, the major types include subtropical monsoon evergreen broad-leaved forest, subtropical evergreen broad-leaved forest, coniferous and broad-leaved mixed forest, bamboo and shrub grass, etc. (Li et al., 2005). The observation data are provided by Dinghushan Forest Ecosystem Station of Zhaoqing, Chinese Academy of Sciences, which is making active and core measurements presently. The flux tower is set in the sampling plot of "Wukesong" coniferous and broad-leaved mixed forest in Dinghushan (23°10'24"N, 112°32'10E; Fluxnet Site Code: CN-Din) (Figs. 1a, 1c), which has an altitude of 300 meters and a slope of about 10 degrees, the slope to the southeast direction (Wang et al., 2007; Zhang et al., 2010). The dominant specieis *Pinus massoniana*, which was planted in 1930-1950, because of the invasion of *Lindera metcalfiana*, *Castanopsis chinensis* and *Cryptocarya concinna*, it formed a semi-natural forest through secondary succession (Zhou et al., 2004; Wang et al., 2007) (Fig. 1b). Vegetation community structure can be divided into four layers: two sub-layers of trees, shrub layer, herbs and seedlings layer (Shi et al., 2006). Leaf Area Index (LAI) was 4.0, which ranges from 3.7 to 4.2.

b. Methods

The flux tower is divided into the ground part and the underground part. The ground part is divided into 7 layers, with the heights of 4 m, 9 m, 15 m, 21 m, 27 m, 31 m and 36 m respectively (Fig. 2). The micrometeorological data was measured in the period from 1 August to 30 September 2015, including average data per 30 min and 10 Hz pulsation data. The observed data were listed in the Table 1 and dry deposition single-point model forcing data included wind speed, wind direction, air temperature, relative humidity, atmospheric pressure, downward longwave radiation, downward shortwave radiation and rainfall. Latent heat flux (LH), sensible heat flux

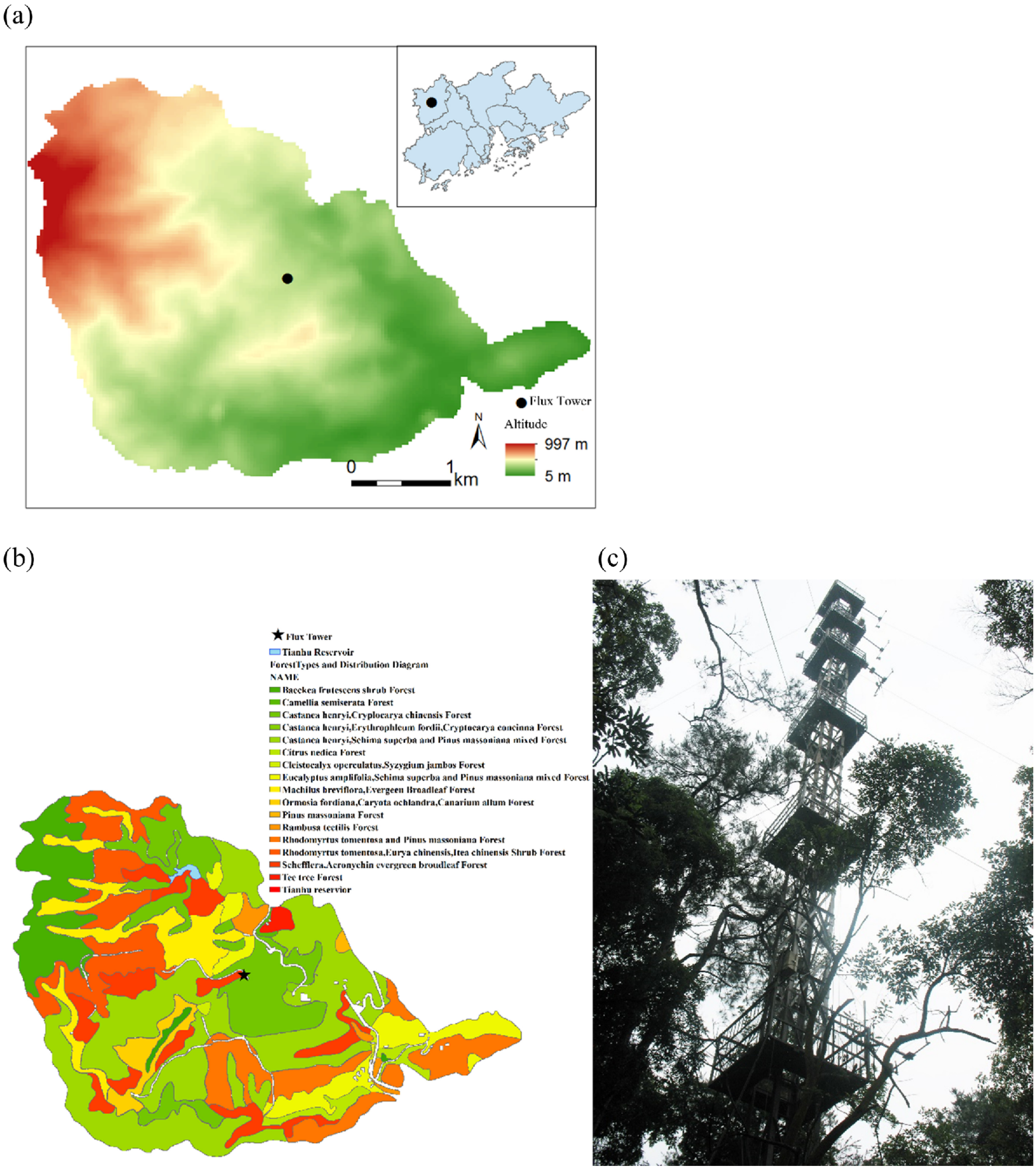

Fig. 1. Observation area and observation site in Dinghushan: (a) Observation area location, (b) Forest types and distribution diagram, (c) photo of a flux tower.

(SH), soil heat flux (G), net radiation (Rn) were used to validate the model performance.

The NO_x concentration was measured using a NO_x analyzer (Model T200, Teledyne-API, USA). The dry deposition velocity V_d was calculated by using the concentration difference between canopy interior and canopy exterior. The experiment was carried out in the period with the lushest vegetation growth from 1 August to 30 September 2015, during which the NO_x concentration difference between canopy interior and canopy exterior is relatively larger due to more foliage of plants blocking the deposition of the gaseous substances. The V_d and flux of NO_x were calculated by eddy-correlation method and aerodynamic gradient method (Wu et al., 2015). It assumes that turbulent transport is comparable with a molecular diffusion motion, the gradient theory of flux can be expressed as the following equation.

$$F = -K_c\, dC/dz \tag{1}$$

K_c represents the eddy current diffusion coefficient of the gas; and dC/dz represents the vertical concentration gradient of the gas substance.

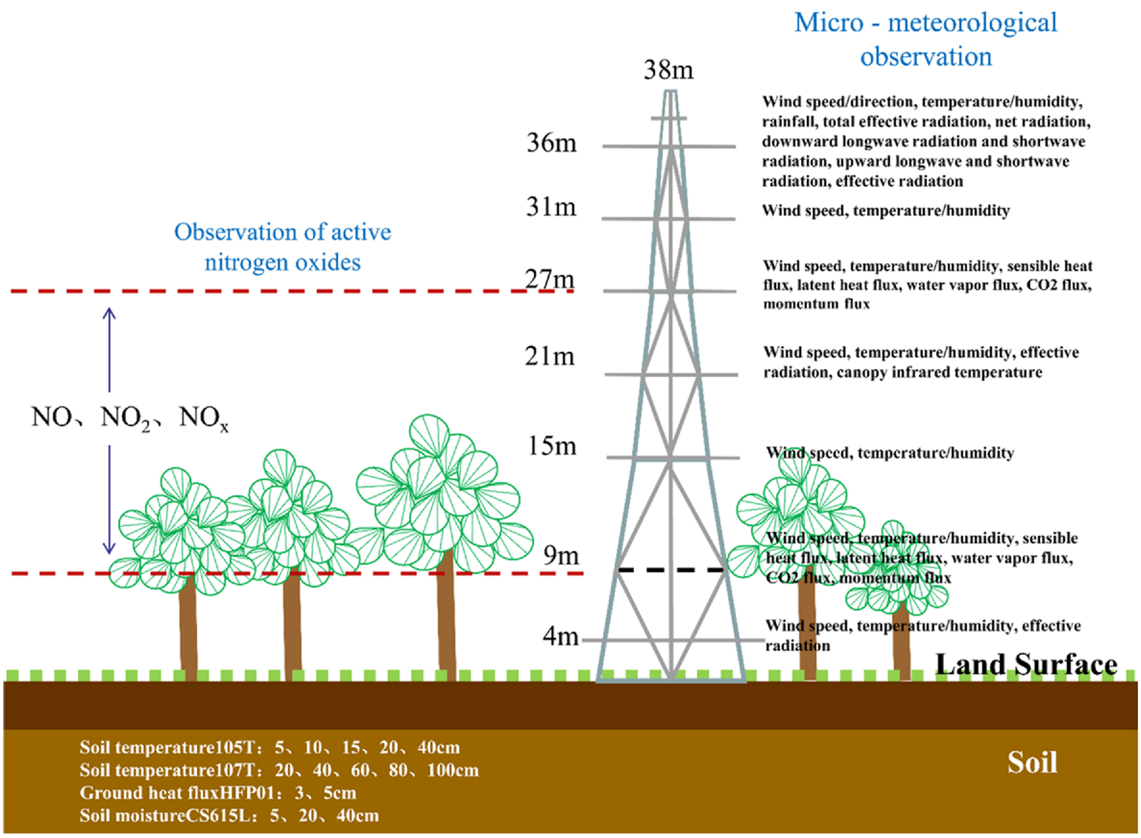

Fig. 2. Schematic diagram of the flux tower in Dinghushan.

Table 1. Observation information of the meteorological data observation

Item	Unit	Method	Height ("-" indicates that the observation is located below the surface.)	Frequency	Raw sampling rate
Sensible heat flux	W m^{-2}	Eddy covariance	9 m, 27 m	sec, 30 min.	10Hz
Latent heat flux	W m^{-2}	Eddy covariance	9 m, 27 m	sec, 30 min.	10Hz
Ground heat flux	W m^{-2}	Sensor	−5 cm	30 min.	
Downward longwave radiation	W m^{-2}	Sensor	36 m	30 min.	
Downward shortwave radiation	W m^{-2}	Sensor	36 m	30 min.	
Upward longwave radiation	W m^{-2}	Sensor	36 m	30 min.	
Upward shortwave radiation	W m^{-2}	Sensor	36 m	30 min.	
Net radiation	W m^{-2}	Sensor	36 m	30 min.	
Air temperature	°C	Sensor	15 m,	30 min.	
Relative humidity	%	Sensor	15 m	30 min.	
Wind direction	degree	Sensor	15 m	30 min.	
Wind speed	M s^{-1}	Sensor	15 m	30 min.	
Pressure	kPa	Sensor	4 m	30 min.	
Precipitation	mm	Sensor	36 m	30 min.	
Soil temperature	°C	Sensor	−5 cm, −10 cm, −20 cm, −40 cm, −60 cm, −100 cm	30 min.	
Soil moisture	m^3 m^{-3}	Sensor	−5 cm, −20 cm, −40 cm	30 min.	

The aerodynamic gradient method assumes that heat and material have the same transport mode on the ideal underlying surface. K_c is closely related to the interstitial aerodynamic resistance (R_a), and the relationship between the two parameters as follows.

$$R_a(z_1{:}z_2) = \int_{z_2}^{z_1} dz/K_c(z) \quad (2)$$

z_1 and z_2 are the heights of canopy exterior and canopy interior near the top of the canopy, and $z_1 > z_2$. According to the above two equations, the gas deposition flux (F) can be expressed as follows.

$$F = -\frac{\Delta C}{R_a(z_1{:}z_2)} = -\frac{C_1 - C_2}{R_a(z_1{:}z_2)} \quad (3)$$

C_1 and C_2 are the gas concentrations corresponding to the height of z_1 and z_2.

R_a is calculated as follows.

$$R_a(z_1:z_2) = (\kappa u_*)^{-1}[\ln\frac{z_1-d}{z_2-d} + \psi_h(\frac{z_1-d}{L}) - \psi_h(\frac{z_2-d}{L})] \quad (4)$$

κ is the Karman constant, 0.4; u_* is the friction velocity measured at the corresponding height; d is the height of the zero-plane displacement; L is the Monin-Obukhov length; and ψ_h is the integrated stable callback function for the heat distribution. u_*, d, L are calculated as follows.

$$u_* = [(\overline{u'w'})^2 + (\overline{v'w'})^2]^{1/4} \quad (5)$$

$$d = h \times (0.1 + LAI^{0.2}/2) \quad (6)$$

$$L = -Cp \times R_a \times u_*^3 \times thet/SH/\kappa/g \quad (7)$$

h is the canopy height, 17 m.

V_d of the gas is calculated according to the following formula.

$$V_d(z) = F/C(z) \quad (8)$$

3. Description of models

a. Noah-MP land surface model

Noah-MP land surface model is developed based on the Noah Land Surface Model (Noah LSM), with multiple parameterization options to simulate the energy, momentum and material interactions in the vegetation-soil-atmosphere system. The options are shown in Table 2. Based on the comprehensive process of water and heat coupled in Noah LSM, a vegetation canopy with self - defined height, canopy radius, density and radiation characteristics was built in Noah-MP (Niu et al., 2011), and a two-stream radiation transfer scheme (Yang and Friedl, 2003; Niu and Yang, 2004) with sufficient consideration of canopy shading effect, rain and snow process, internal water and heat transfer and other conditions was introduced in Noah-MP. Moreover, a TOPMODEL-based runoff scheme (Niu et al., 2005, 2007) was also implemented in the Noah-MP, and a dynamic vegetation growth model (Dickinson et al., 1998) was used to simulate the physiological processes of vegetation. The processes mentioned above were coupled together to make up for the shortcomings of the Noah LSM in over-simplifying the interaction between vegetation, soil and hydrology. Noah-MP, which is driven by the meteorological data, vegetation and soil parameters, to calculate the phenological and turbulent characteristics, the energy and moisture distribution of the land surface during each time step according to the physical parameterization scheme (Chen et al., 2014; Gao et al., 2015). Finally, the outputs of model include water storage of land surface processes (e.g. soil moisture, snow cover height, etc.), and reflected and absorbed shortwave and

Table 2. Physical processes scheme options.

Physical parameterization scheme	Options	Contents
Vegetation Model (DVEG)	1	Prescribed (table LAI, shadow fraction = FVEG)
	2	Dynamic
	3	Table LAI, calculated FVEG
	4	Table LAI, shadow fraction = maximum.
Canopy Stomatal Resistance (CRS)	1	Ball-Berry scheme
	2	Jarvis scheme
Soil moisture factor for stomatal resistance, β Factor (BTR)	1	Noah scheme
	2	CLM scheme
	3	SSiB scheme
Runoff and Groundwater (RUN)	1	SIMGM scheme
	2	SIMTOP scheme
	3	Schaake96 scheme
	4	BATS scheme
Surface Exchange Coefficient for Heat, C_H (SFC)	1	M-O scheme
	2	Chen97 scheme
Supercoiled Liquid Water in Frozen Soil (FRZ)	1	NY06 scheme
	2	Koren99 scheme
Frozen Soil Permeability (INF)	1	NY06 scheme
	2	Koren99 scheme
Radiation Transfer (RAD)	1	Three - dimensional canopy morphology
	2	Vegetation gap = 0
	3	Vegetation gap = 1-FVEG
Snow Surface Albedo (ALB)	1	BATS scheme
	2	CLASS scheme
Partitioning Precipitation into Rainfall and Snowfall (SNF)	1	Jardan91 scheme
	2	BATS scheme
	3	Noah scheme
Lower Boundary of Soil Temperature (TBOT)	1	Zero-flux scheme
	2	Noah scheme
Snow/Soil Temperature Time Scheme (STC)	1	Semi-implicit
	2	Fully implicit

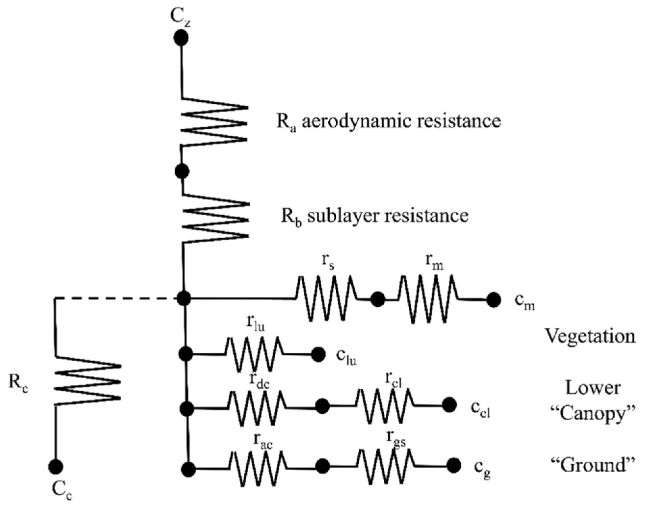

Fig. 3. Dry deposition resistance components (Wesely, 1989).

longwave radiation fluxes, heat flux, latent heat flux of evaporation and transpiration, the temperature of surface, vegetation canopy and other locations, and the carbon flux and carbon storage, which provide the physical input data for WDDM.

b. WRF-Chem Dry Deposition Module (WDDM)

The calculation of the V_d in WDDM is based on the Wesely scheme (Wesely, 1989). The dry deposition of gaseous matter is divided into three parts, turbulent diffusion, molecular diffusion and absorption at external and internal plant parts. In addition, there are different levels of resistances for the three processes, such as the aerodynamic resistance (R_a), quasi-laminar sub-layer resistance (R_b) and surface resistance (R_c) (Erisman and Draaijers, 2003) (Fig. 3). The Wesley scheme defines V_d as the reciprocal of the total resistance (R_t), which produced in the process of the dry deposition of the gas from the atmosphere to the receptor surface (Wesely, 1989). It's calculated as the following equation.

$$V_d(z) = R_t^{-1} = \left(R_a(z) + R_b + R_c\right)^{-1} \tag{9}$$

The calculation of R_a is divided into three cases as follows (Mcrae, 1982).

$$R_a = 0.74(\kappa u_*)^{-1}[\ln(z/z_0) + 4.7(z - z_0)/L] \text{ (steady conditions)} \tag{10}$$

$$R_a = 0.74(\kappa u_*)^{-1}\ln(z/z_0) \text{ (neutral conditions)} \tag{11}$$

$$R_a = 0.74(\kappa u_*)^{-1}\{\ln[\frac{(1-9z/L)^{0.5}-1}{(1-9z/L)^{0.5}+1}] - \ln[\frac{(1-9z_0/L)^{0.5}-1}{(1-9z_0/L)^{0.5}+1}]\}$$

(unstable conditions) (12)

R_b is calculated as follows.

$$R_b = 2(\kappa u_*)^{-1}(S_c/P_r)^{2/3} \tag{13}$$

S_c is the Schmidt constant, which is related to the temperature and the radius of the gas molecule, and P_r is the Prandtl constant of the air, 0.72.

R_c is the most complex and computationally difficult part of the resistance, which varies with the nature of the land surface and the characteristics of gas species. When the solar radiation and daytime temperature increases (SH increases), the R_c will be significantly reduced, so that the dry deposition rate significantly increases. While when the forest evapotranspiration increases, the water consumption will increase (LH increases), the soil moisture is reduced, resulting the plant stomatal closure and the growth of R_c (Erisman and Draaijers, 2003). R_c is the most important factor affecting the $V_d(NO_x)$, and the calculation is as follows.

$$R_c = \left(\frac{1}{R_s + R_m} + \frac{1}{R_{lu}} + \frac{1}{R_{dc} + R_{cl}} + \frac{1}{R_{ac} + R_{gs}}\right)^{-1} \tag{14}$$

R_s is the stomatal resistance of the leaves in the canopy, mainly due to the diffusion of gaseous material through the stomata of the leaves, which can occur simultaneously on both sides of the leaf; R_m is the mesophyll resistance, R_{lu} is the epidermal resistance of the healthy vegetative leaf surface, and they are mainly determined by the position in the canopy; R_{dc} is the meteorological transmission resistance caused by the buoyancy in the canopy, and R_{cl} is the surface resistance of leaves and bark; R_{ac} is the resistance at the top of the canopy to the receptor surface, and R_{gs} is the surface resistance of the cover, such as soil and litter.

Wesely (1989) used a simple empirical formula to compute the change of R_s.

$$R_s = R_i\{1 + \frac{1}{[200(G+0.1)]^2}\}\frac{400}{T_s(40-T_s)}\frac{D_{H_2O}}{D_x} \tag{15}$$

R_i is the minimum canopy stomatal resistance, G is the solar radiation, T_s is the surface temperature (^{o}C), D_x is the molecular diffusion rate of the contaminating gas molecules, and D_{H_2O} is the molecular diffusion rate of the water vapor molecule. And when T_s is less than 0^{o}C or more than 40^{o}C, R_s is 9999. The canopy stomatal resistance (R_s) mainly depends on the size of the stomata, and the opening or closing of the stomata mainly depends on the photosynthesis needs of the plants. The stomata can control the gas exchange between the leaves and the atmosphere. It is generally believed that the diffusion resistance of the stomata for the gas increases as the temperature decreases (Berry and Raison, 1981). It has been reported that the response of the stomata to the temperature is related to the state of the water in the plant, but other studies have shown that low temperature conditions do not cause changes in the plant's water, but the stomata remains closed (Brix, 1962). Under high temperature conditions, the plant may first control the passage of the CO_2 into the photosynthetic reaction site by adjusting the stomata size or closing the stomata to protect the photosynthetic reaction site from high temperature damage (Taub et al., 2000). Thus, the extreme conditions of 0°C and 40°C cause plant photosynthesis to be blocked and even cause irreversible damage to the plant, and the leaf stomata are closed, so R_s is set to 9999.

Noah-MP also has two options to calculate canopy resistance R_s: 1) Jarvis scheme, and 2) Ball-Berry scheme. Jarvis's equation is fairly similar to Wesely's Eq. (15), while Ball-Berry scheme is a more complex scheme. The Jarvis scheme is based on the fitting stress equation of environmental effects such as photosynthetically active radiation, temperature, humidity and soil moisture, to calculate the canopy resistance R_c (Jarvis, 1976), which is calculated as follows:

$$R_c = \frac{R_{smin}}{R_{cs} \times R_{ct} \times R_{cq} \times R_{csoil}} \tag{16}$$

In Eq. (16), R_{smin} is the minimum stomatal resistance parameter, R_{cs} is the radiation stress coefficient, R_{ct} is the temperature stress coefficient, R_{cq} is the water vapor pressure stress coefficient, and the equations are as follows:

$$R_{cs} = \frac{\frac{2 \times PAR}{RGL} + \frac{R_{smin}}{R_{smax}}}{1 + \frac{2 \times PAR}{RGL}} \tag{17}$$

$$R_{ct} = 1 - 0.0016 \times (T_{top} - T_{sfc})^2 \tag{18}$$

$$R_{cq} = \frac{1}{1 + HS \times max\{q2sat - q2, 0\}} \tag{19}$$

PAR is the photosynthetically active radiation, *RGL* is the radiation efficiency parameter, R_{smax} is the maximum stomatal resistance parameter, T_{top} is the maximum transpiration efficiency temperature, T_{sfc} is the air temperature at the observation height, *HS* is the vapor pressure loss parameter, *q2sat* is the saturated water vapor mixture ratio, and R_{csoil} is the coefficient of soil water stress (calculated from the soil water potential process).

The Ball-Berry scheme is based on the CO_2 concentration and humidity of the blade surface, it is calculated in conjunction with the rate of photosynthesis in the dynamic vegetation process (Ball et al., 1987, Collatz et al., 1991). The equation for calculating canopy stomatal resistance is:

$$\frac{1}{R_s} = m \times \frac{A}{c_{air}} \times \frac{e_{air}}{e_{sat}(T_v)} \times P_{air} + g_{min} \tag{20}$$

In Eq. (20), *m* is the slope of the stomatal conductance (9.0 in the model), *A* is the photosynthetic rate (provided by the dynamic vegetation scheme), C_{air} is the CO_2 concentration on the leaf surface, e_{air} is the vapor pressure on the blade surface, *sat* (T_v) is the saturated vapor pressure of the leaves at the canopy temperature, P_{air} is the surface pressure, and g_{min} is the minimum stomatal conductance.

Although the two schemes in this process are parameterized directly for the calculation of canopy stomatal resistance and affect the dry deposition velocity, they are affected by other processes and may be difficult to adequately show their difference in short-term simulations (Kumar et al., 2014). The Jarvis scheme, although it is an earlier complete canopy re-

Table 3. Resistance Parameters of Gas Deposition in Forest Area in Summer (s m^{-1}), (Wesely, 1989). No exchange between land and atmosphere is indicated by 9999.

Resistance component	Land use types		
	4 (Deciduous forest)	5 (Coniferous forest)	6 (Mixed forest containing wetland.)
Season Type 1: Summer (with lush vegetation)			
R_i	70	130	100
R_{lu}	2000	2000	2000
R_{ac}	2000	2000	2000
$R_{gs}S$	500	500	100
$R_{gs}O$	200	200	300
$R_{cl}S$	2000	2000	2000
$R_{cl}O$	1000	1000	1000
Season Type 2: Autumn (with crop not harvested)			
R_i	9999	250	500
R_{lu}	9000	4000	8000
R_{ac}	1500	2000	1700
$R_{gs}S$	500	500	100
$R_{gs}O$	200	200	300
$R_{cl}S$	9000	2000	4000
$R_{cl}O$	400	1000	600
Season Type 3: late autumn after frost (without snow cover)			
R_i	9999	250	500
R_{lu}	9000	4000	8000
R_{ac}	1000	2000	1500
$R_{gs}S$	500	500	200
$R_{gs}O$	200	200	300
$R_{cl}S$	9000	3000	6000
$R_{cl}O$	400	1000	600
Season Type 4: Winter (no snow, below freezing)			
R_i	9999	400	800
R_{lu}	9999	6000	9000
R_{ac}	1000	2000	1500
$R_{gs}S$	100	100	100
$R_{gs}O$	3500	3500	3500
$R_{cl}S$	9000	200	400
$R_{cl}O$	400	1500	600
Season Type 5: Spring (with some dwarf green plants)			
R_i	140	250	190
R_{lu}	4000	2000	3000
R_{ac}	1200	2000	1500
$R_{gs}S$	500	500	200
$R_{gs}O$	200	200	300
$R_{cl}S$	4000	2000	3000
$R_{cl}O$	500	1500	700

sistance model, creates a condition for systematically studying the mechanism of canopy stomatal resistance by external environmental changes. This model also has some drawbacks: most of the parameters in the model are not biologically (Li et al., 2011), and only for the independent effects of environmental factors on stomatal resistance, ignoring the synergistic or interaction between the factors (H. S. Niu et al., 2005). In addition, since the Jarvis scheme coupled to Noah-MP does not consider vegetation physiology and ecological processes, the Ball-Berry scheme must be selected when the vegetation physical process is a dynamic vegetation (Niu et al., 2011).

The other components of surface resistance (R_c) are mostly related to the solubility and oxidation activity of pollutants. Water-soluble and oxidative gas is easier to deposit to the receptor surface.

$$R_m = \left(H^* / 3000 + 100 f_0\right)^{-1} \tag{21}$$

H^* is the effective Henry constant, f_0 is the reactive factor.

The cuticle resistance (R_{lu}) of the leaves is treated according to the dry and wet conditions of the canopy surface. When the canopy surface is dry,

$$R_{lu,dry} = R_{lu}\left(10^{-5} H^* + f_0\right)^{-1} \tag{22}$$

R_{lu} can be found in the Table 3. For the wet canopy surface, the R_{lu} of SO_2 in the urban underlying surface is uniformly set to $50\ \mathrm{s \cdot m^{-1}}$, and $100\ \mathrm{s \cdot m^{-1}}$ for the other. The R_{lu} of O_3 is calculated as follows.

$$R_{lu,o_3,dew} = \left(1/3000 + 1/(3R_{lu})\right)^{-1} \tag{23}$$

R_{lu} of other contaminants is given below.

$$R_{lu,dew} = \left(1/(3R_{lu,dry}) + 10^{-7} H^* + f_0 / R_{lu,o_3,dew}\right)^{-1} \tag{24}$$

The atmospheric buoyancy resistance (R_{dc}) in the vegetation canopy depends mainly on the slope of the terrain and the heating of the surface by solar radiation.

$$R_{dc} = \frac{100\left(1 + \frac{1000}{G + 10}\right)}{1 + 1000\theta} \tag{25}$$

θ is the terrain slope.

R_{cl} of SO_2 and O_3 are obtained from the Table 3, while other contaminants are calculated according to the water solubility and oxidation of the gas.

$$R_{cl} = \left(\frac{10^{-5} H^*}{R_{cl,so_2}} + \frac{f_0}{R_{cl,o_3}}\right)^{-1} \tag{26}$$

Similar to R_{cl}, R_{gs} is calculated as follows. R_{ac} can be obtained the Table 3.

$$R_{gs,x} = \left(\frac{10^{-5} H^*}{R_{gs,so_2}} + \frac{f_0}{R_{gs,o_3}}\right)^{-1} \tag{27}$$

c. Model configurations

In order to reduce the effect of meteorological simulation biases on V_d simulation, V_d (NO_x) was calculated by using meteorological observation data to drive Noah-MP-WDDM dry deposition single-point model. The physical processes, related to snow, permafrost and other factors, such as FRZ (Supercoiled Liquid Water in Frozen Soil), INF (Frozen Soil Permeability), ALB (Snow Surface Albedo), SNF (Partitioning Precipitation into Rainfall and Snowfall), TBOT (Lower Boundary of Soil Temperature) and STC (Snow/Soil Temperature Time Scheme), which only play a little effect on V_d because the study area is located in the subtropics. Option 1 is selected in the above physical parameterization scheme. While the other six physical parameterization schemes of DVEG (Vegetation Model), CRS (Canopy Stomatal Resistance), BTR (Soil moisture factor for stomatal resistance, β Factor), RUN (Runoff and Groundwater), SFC (Surface Exchange Coefficient for Heat, C_H) and RAD (Radiation Transfer) have great

Table 4. The model configurations.

Parameters	Designated value
Start date	UTC Time, 201507311600
End date	UTC Time, 201509301530
Loop for a while	20
Latitude (°)	23.17
Longitude (°)	112.53
Forcing Time step (s)	1800
Noah LSM Time step (s)	900
Sea ice point	. FALSE.
Soil layer thickness (m)	0.1, 0.2, 0.6, 1.0.
Soil Temperature (K)	298.3708, 298.2593, 298.1231, 297.2400
Soil Moisture ($\mathrm{m^3 \cdot m^{-3}}$)	0.2185000, 0.2359500, 0.2534000, 0.2536000
Soil Liquid ($\mathrm{m^3 \cdot m^{-3}}$)	0.1611681, 0.2359500, 0.2534000, 0.2536000 (Default)
Skin Temperature (K)	304.2858
Canopy water	3.9353027E-04 (Default)
Snow depth (m)	1.0600531E-03 (Default)
Snow equivalent	2.0956997E-04 (Default)
Deep Soil Temperature	297.2400 (Soil temperature at 1 m depth)
Land use dataset	"USGS"
Vegetation type index	15 (Mixed Forest)
Soil type index	2 (Loamy sand)
Urban vegetation category	1 (Default)
Glacial vegetation category	24 (Default)
Slope type index	1
Air temperature level (m)	4.0
Wind level (m)	15.0
Shadow fraction monthly	0.98

influence on V_d simulation. They have the above 4, 2, 3, 3, 2 and 3 options respectively. Based on the above information, a total of 576 parametric combinations of physical processes were obtained by orthogonal method, according to which the model will produce 576 simulation results, the model output frequency is 30 minutes. The output data includes V_d (NO_x), deposition resistance, energy balance components, radiation flux components, weather-driven data, etc. It's also necessary to set the model configuration to represent the actual forest conditions in Dinghushan, including the time of the start and the end of the simulation, the simulated position coordinates, the land cover type, the soil type and properties (soil layer thickness, soil temperature, soil moisture, soil liquid, skin temperature and deep soil temperature), the height of the observation (air temperature level, wind level). However, as mentioned earlier, this study area is located in the subtropical region. Therefore, the forcing (snow depth, snow equivalent and sea ice point) related to snow and sea ice point are assigned to default values of Noah-MP. Table 4 lists the setting of specific model configuration. In addition, model spin-up is the process through which the model is adequately equilibrated to ensure balance between the mass fields and velocity fields. Setting loops is to skip spin-up. And our experiments showed that when loop is set to 20, the simulation results can be stable. The setting of time step is based on the time frequency of the observed data.

4. Results and discussion

a. Analysis of observation results

V_d(NO_x) was measured using the eddy covariance method and aerodynamic gradient methods described previously. The data measured by eddy covariance method are affected greatly by the turbulence intensity. When the turbulence is weak, the accuracy of the measurement result will be affected. From the wind speed profile of Dinghushan (Fig. 4), it can be clearly seen that the wind speed in the canopy is slower than that outside the canopy. In the canopy, the night wind speed is slower than the wind speed during the day. Outside the canopy, however, the situation is reversed. The above phenomenon is because the canopy and the surrounding terrain together make the radiation distribution of the layer is more uniform. Especially at night, the canopy air flow is difficult to develop, resulting in the weak wind. There will be valley wind outside the canopy in evening, the airflow is almost unaffected by the vegetation outside the canopy, so the wind speed increased dramatically. Apparently, the wind speed inside and outside the canopy is different, and it shows significant diurnal variation. And during stable night-time conditions, the uncertainty of the flux observation comes from the lack of the turbulence. The friction velocity (u^*) can be used as an important index to judge the turbulence mixing intensity. The larger u^* is, the greater the turbulence intensity is. Aubinet (2000) found that deleting the carbon flux at low u^* can effectively improve the

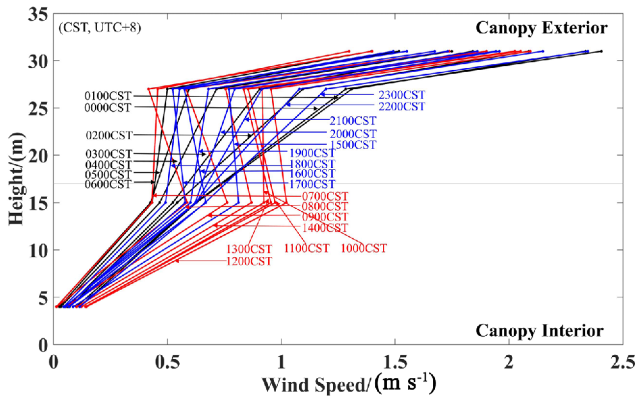

Fig. 4. The wind speed (m s^{-1}) profile in Dinghushan from 1 August to 30 September, 2015.

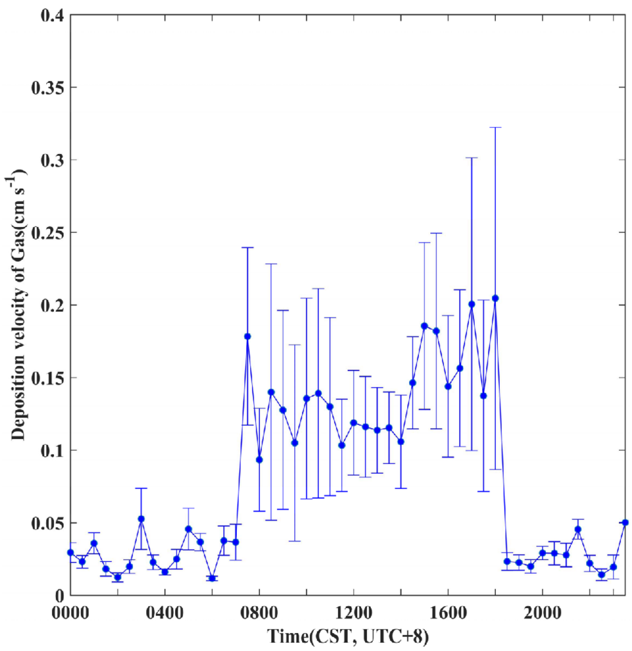

Fig. 5. The diurnal variation of observed V_d (NO_x) (cm s^{-1}) in Dinghushan. The vertical bar is the standard deviation of the data.

exponential relationship between nighttime carbon flux and temperature. In order to ensure the reliability of the data, the observation data with small u^* were excluded in this study (Li et al., 2005). By dividing the frequency, a threshold (0.15 m s^{-1}) of u^* is determined (Bi et al., 2007). If the u^* is greater than this threshold, the turbulence intensity is considered and the flux data is valid.

The inspection instrument Model T200 used for observation is required to run in a ventilated environment, so that the gas has been assayed in chamber can be discharged in time to ensure the accuracy of the next sample test results. But the instrument is limited by the conditions surrounding the flux tower, the gas has been assayed accumulated (especially at night) in the reaction chamber, resulting in a partial (nocturnal) high observed value. In order to improve the reliability of the

Table 5. Summary of the observation results in this study and other studies.

Site	Land use types	Observation period	$V_d(NO_x)$/(cm s^{-1})	References
Dinghushan forest, southern China	Forest	2015.8-2015.9	0.012-0.20	This study
Xibeiwang Town in Beijing City, China; Quzhou, Hebei Province, China	Urban; Agriculture	2007.10-2008.9	0.59	Shen et al., 2009
Norway	Patchy land with bare rock and low grass	2003-2007	1.2	Hole et al., 2008
Yingtan, Jiangxi Province, China	Agriculture	2005-2006	0.07-0.24	Cui et al., 2010
Yingtan, Jiangxi Province, China	Agriculture	2004.1-2014.12	0-0.30	Fan et al., 2009
Nanjing City, Jiangsu Province, China	Urban	2005.6-2006.5	0.12	Deng et al., 2009
Scherzheim	A flat area with mixed farming and patches of forest	1992.9.11-22	0.014 0.0017	Pilegaard et al., 1998

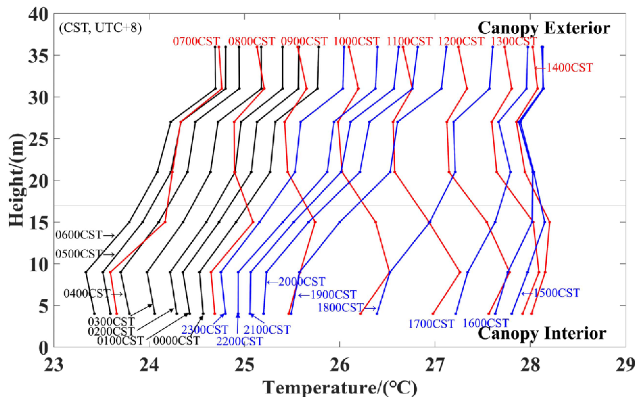

Fig. 6. The temperature (°C) profile in Dinghushan from 1 August 2015 to 30 September 2015.

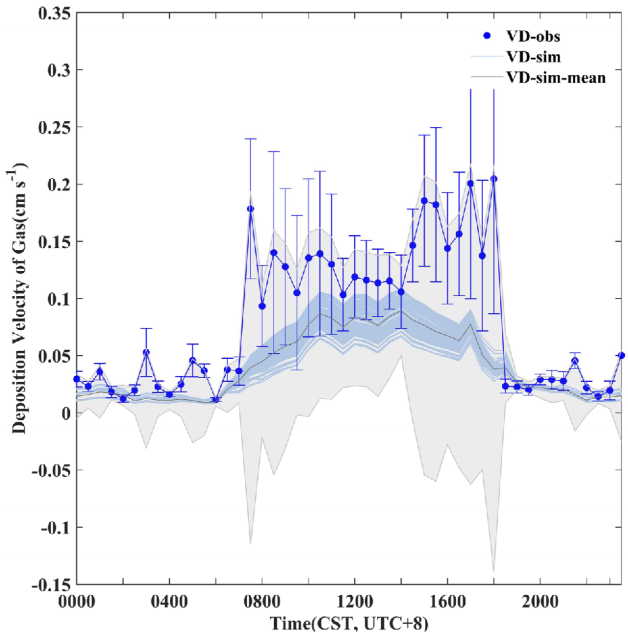

Fig. 7. Comparison of simulated V_d (NO_x) values (cm s^{-1}) and observed V_d (NO_x) values (cm s^{-1}) from 1 August to 30 September 2015. The vertical bar is the standard deviation of the observed data and the shaded portion represents the standard deviation of simulated data.

data, we also excluded the abnormally high value of nighttime observation.

Figure 5 shows the diurnal variation of $V_d(NO_x)$ after unreasonable data was removed, and the variation range is 0.012-0.20 cm s^{-1}, which is close to that of other studies (Table 5). It can be seen from Fig. 5 that V_d (NO_x) fluctuates at night, and the nighttime V_d (NO_x) is obviously lower than daytime. It is well known that the spatial vertical distribution of the temperature in lower atmosphere has the most direct effect on the processes of atmospheric deposition and diffusion (Liu et al., 2005). Therefore, it can be seen from the diurnal variation of the temperature profile of Dinghushan (Fig. 6) that the inversion of temperature occurs at all times whether in the canopy or outside the canopy, but it is stronger inside the canopy and night temperature inversion is stronger than that of day.

A large amount of vegetation and low mountains surrounding the flux tower, resulting in the emergency of the above phenomenon. Because of the sheltering effect of the vegetation, the solar radiation reaching the surface is greatly reduced, the surface temperature is low, and the obstruction of the vegetation to the air flow makes the lower atmosphere cannot be fully mixed by the turbulence. So the temperature inversion occurs in the canopy. Outside the canopy, the atmosphere is free from the effects of vegetation, but at night, the cold air on the hillside can sink, and the original warm air is lifted to form the terrain inversion. In the inverse temperature conditions, the vertical movement of the air mass is inhibited, and V_d (NO_x) is reduced accordingly. Hence, V_d (NO_x) in the day was significantly higher than that in the night. In addition, the observed V_d (NO_x) shows high values and peaks in the period of 0730 CST (China Standard Time, which is UTC+8:00)-0800 CST and 1500 CST-1900 CST, which is probably due to the emission and transportation of local sources and the release of contaminants at nighttime in the boundary layer.

b. Analysis of simulation results

The simulation results are compared with the observed V_d

Table 6. The combination of the key physical processes.

Physical parameterization scheme	Option	Content
DVEG	3	Table LAI, calculated FVEG
CRS	2	Jarvis Scheme
BTR	1	Noah Scheme
RUN	1	SIMGM Scheme
SFC	2	Chen97 Scheme
FRZ	1	NY06 Scheme
INF	1	NY06 Scheme
RAD	2	Vegetation gap = 0
ALB	1	BATS Scheme
SNF	1	Jardan91 Scheme
TBOT	1	Zero-flux Scheme
STC	1	Fully implicit

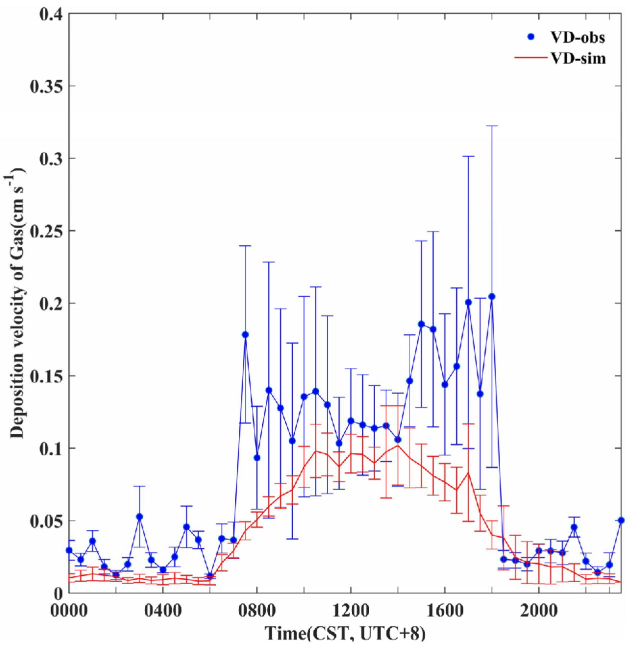

Fig. 8. Comparison of optimal simulated values and observed values (cm s^{-1}). The vertical bar is the standard deviation of the data.

(NO_x), and the results are shown in Fig. 7. It can be seen that the simulation peak value of V_d (NO_x) is within the range of 0.050-0.10 cm s^{-1}. All of the simulated values are lower than the observed values, but the simulated values and the observed values have the same diurnal trend. We choose the optimal simulation value for comparative analysis. Table 6 lists the optimal combination of the key parameterization schemes.

The so-called optimal results, that is, the numerical value and trend are closest to the observed values. Figure 8 displays the comparison of the optimal simulated values and the observed values. The optimal simulated values (0.0075-0.10 cm s^{-1}) are lower than the observed values, but they have the same trend. The nighttime values are lower, and the jump occurs at 0700 CST, and it is at high value in the period from 1000 CST to 1400 CST. There is a significant decline after 1800 CST. The fluctuation of the observed values is larger than that of the simulated values, which is mainly related to the instrument detection error.

Table 7. Statistical results of simulated values and observed values.

Evaluation Criteria	$V_d(NO_x)$
Mean (Observation)	0.0795
Mean (Simulation)	0.0438
Bias	−0.0357
MRB	−0.410
MAE	0.0365
MRE	0.443
RMSE	0.0524
Correlation coefficient	0.905

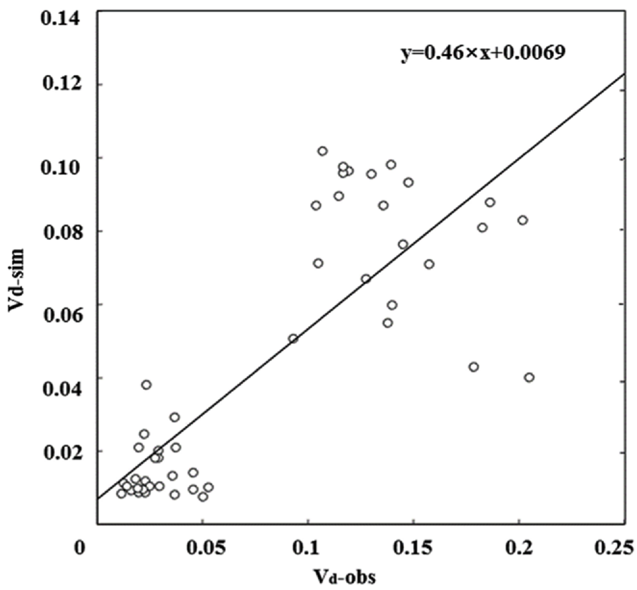

Fig. 9. Fitting of simulated values and observed values of $V_d(NO_x)$.

Further analysis shows that there is a large deviation between the simulation results and the observed results, especially at 0800 CST and 1900 CST, which is related to the transportation of the surrounding pollution sources. Through the comparison results in Table 7, it can be figured out that the average value of the optimal simulation is lower than that of the observation, but the difference is not large. The correlation coefficient of the two results reached 0.905 (Fig. 9). The relationship between the observation and the simulation values is $y = 0.46x + 0.0069$.

Other scholars have also reached a similar conclusion, that is, the use of Wesely scheme underestimated the V_d values. The V_d of atmospheric peroxyacetyl nitrite (PAN), measured by Turnipseed et al. (2006) in the United States conifer forest (Duke Forest) through eddy covariance, was significantly

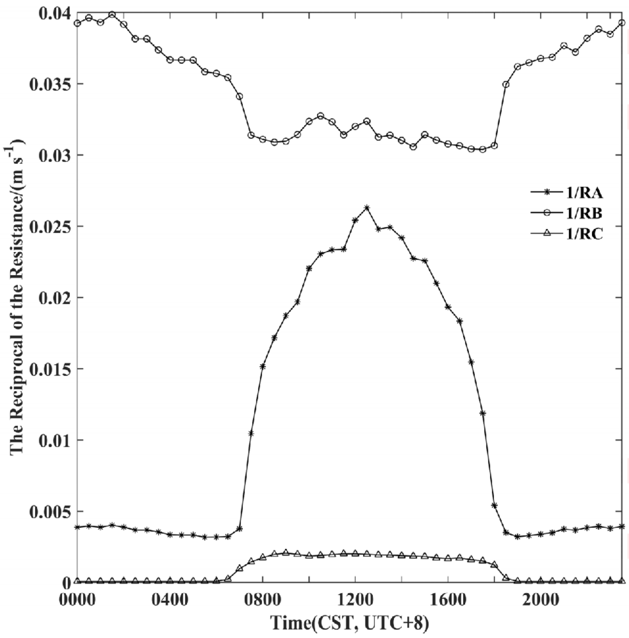

Fig. 10. The diurnal variation of the reciprocal of the key resistance components (m s^{-1}).

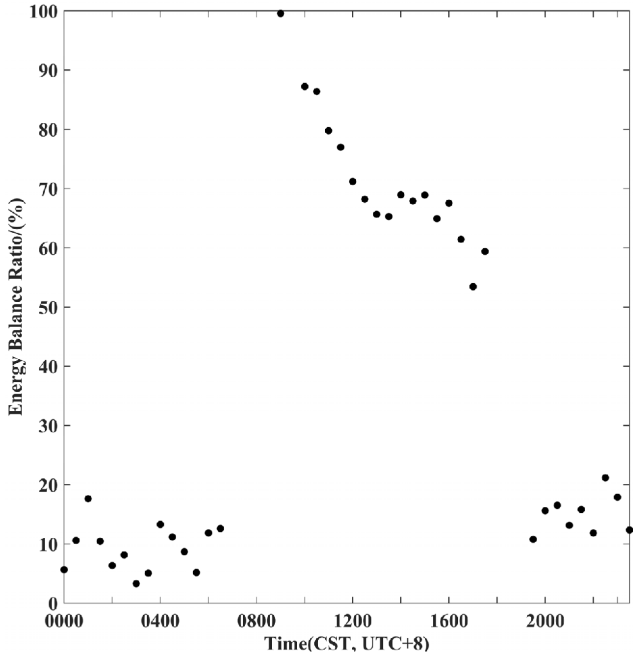

Fig. 12. Diurnal trend of the energy balance ratio.

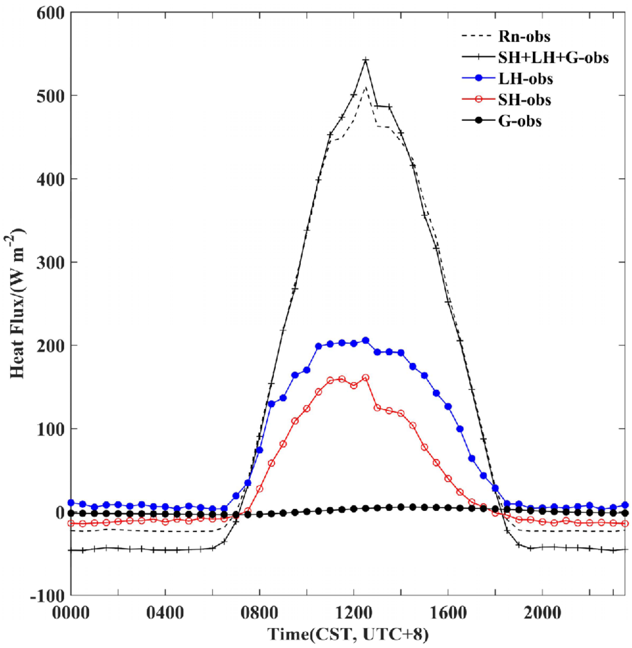

Fig. 11. Diurnal trend of energy components (W m^{-2}).

higher than those simulated by Wesely scheme. Wu et al. (2011) also used the eddy covariance method to observe the V_d (NO_y) in the American deciduous forest (Harvard Forest), and used WDDM to simulate the V_d (NO_y), finding that the model underestimated the V_d (NO_y).

It can be seen from the expression in Section 3b that the calculation of V_d (NO_x) in WDDM through Eq. (9), so that the underestimation of V_d (NO_x) indicates that R_t in WDDM is over-estimated. The main components of R_t include R_a, R_b and R_c. Fig. 10 shows the diurnal variation of the reciprocal of the above three components. It can be seen from the figure that the reciprocal of R_c is the smallest, indicating that it is the most important resistance component for V_d (NO_x). In addition, it has been mentioned in Section 3b that R_c is closely related to LH and SH. Therefore, the detection of the reason for the simulation bias of resistance components is to start from the simulation of the energy components.

Figure 11 shows the diurnal variation of Rn, G, SH and LH, which present significant diurnal variations, and all the curves appear with single peaks at noon. The above three energy components show a negative value at night or close to zero, the change is not significant. But after sunrise, the net radiation begins to show a clear upward trend, the net radiation reached a peak of 542.8 W·m^{-2} at noon. The SH and LH also reach the peak shortly after midday. The change of G in the whole day is not significant, and the order of magnitude is smaller than that of Rn, SH and LH. LH > G > SH at night and LH > SH > G during the daytime, depending on the proportions of the components. And during the daytime, SH and G are positive, indicating that the surface soil and the air is heated. At night, SH are negative but G is positive, indicating that energy is transferred to the soil. In addition, a noteworthy phenomenon is that there is a certain difference between the sum of G, SH, LH and Rn, which means that the energy balance equation is imbalanced. In this study, the energy balance ratio EBR (Energy Balance Ratio), that is, the ratio of turbulent flux to effective energy, is used to evaluate the degree of energy balance of Dinghushan, as shown in Eq. (28).

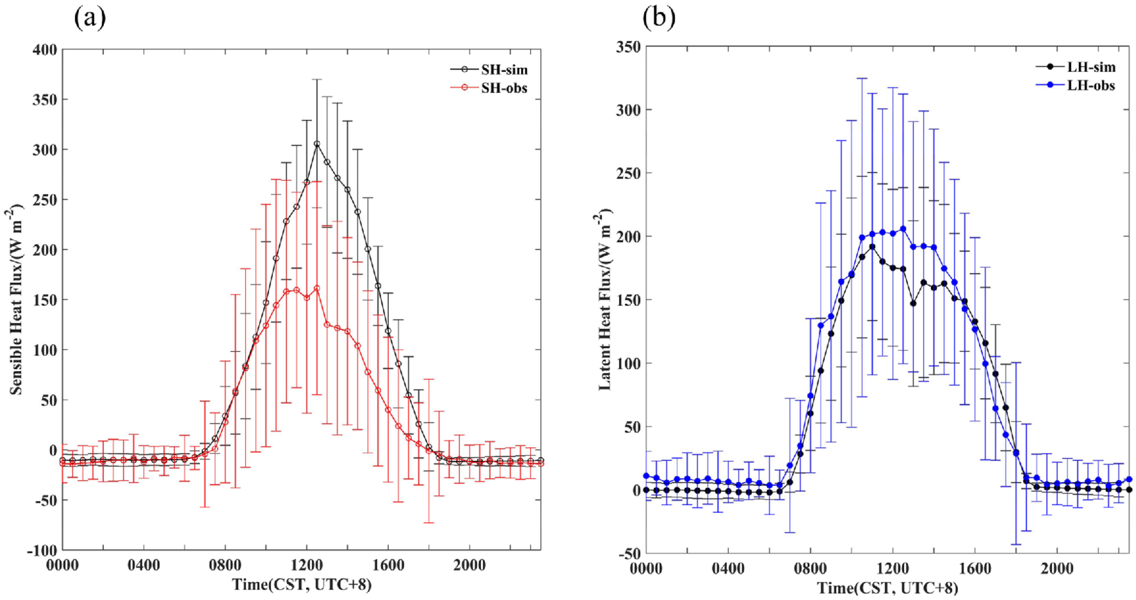

Fig. 13. Comparison of simulated values and observed values: (a) Sensible Heat Flux (W m^{-2}) and (b) Latent Heat Flux (W m^{-2}). The vertical bar is the standard deviation of the data.

Table 8. Statistical results of simulated values and observed values.

Evaluation Criteria	LH	SH
Mean (Observation)	67.7	32.2
Mean (Simulation)	58.6	62.9
Bias	−9.06	30.8
MRB	−0.693	−2.33
MAE	37.1	40.0
MRE	0.746	3.71
RMSE	64.1	75.6
Correlation coefficient	0.887	0.926

$$EBR = \frac{\Sigma(LH+SH)}{\Sigma(Rn-G)} \tag{28}$$

The diurnal variation of EBR is shown in Fig. 12 after eliminating the data with large deviations (EBR > 1 or EBR < 0). It can be seen from Fig. 12 that the degree of energy balance in the day is better than that in the evening, which is in agreement with the findings of many studies (Li et al., 2005; Zuo et al., 2010). There are many reasons for this error. Besides the sampling errors and systematic deviations, the energy storage in the soil-vegetation-atmosphere is not fully taken into account and the turbulence mixing is not enough, causing the above phenomenon. (Li et al., 2005; Zuo et al., 2010).

The differences between the simulation and observation of energy components (SH, LH) are showed in the Fig. 13. The simulated values of SH and LH have the same trend as the observed values. At nighttime, the values are lower and the variation is not significant. After 0700 CST, they all increase significantly and reach the peak at 1200 CST. And after 1700 CST, they restore a stable low value once again. The simulation bias is greater during the day. In addition, SH is overestimated while LH is underestimated. The details of the comparison are shown in Table 8. It can be seen from Table 8 that the simulation of SH is not as good as the simulation of LH. The deviation of SH simulation value is more obvious than that of latent heat.

In order to explore the cause of the bias, we compared the mean values of 576 simulated results of LH and SH with the observed mean values. As shown in Fig. 14, it can be seen that the observed value of LH is within the range of the simulation value, which means that the simulation of LH can be improved by changing the physical option. Therefore, the simulation biases of LH are mainly caused by the option combination. However, the observed value of SH is significantly lower than the range of simulation values. Changing the combination of the options cannot improve the simulation of SH. The bias is mainly due to the fact that the model cannot simulate the surface energy imbalance well. The energy in the soil-vegetation-atmosphere is classified as SH, which leads to the overestimation of SH. This is caused by the parameterization scheme of the model itself. Horton et al. (1996) found that partial surface mulch cover could affect the soil physical environment near the soil surface dramatically. Both measurements and simulations showed that the surface energy balance achieves closure well over dry hot surfaces while other types of land surface are often accompanied by energy imbalance. Lee (1998) concluded that energy imbalance is caused by the energy advection through investigating the exchange process of surface-air system over tall vegetation. Gao et al. (2007) think that energy advection in the land surface with high vegetation is particularly significant. The energy of this part is often difficult to measure due to the limitations of the obser-

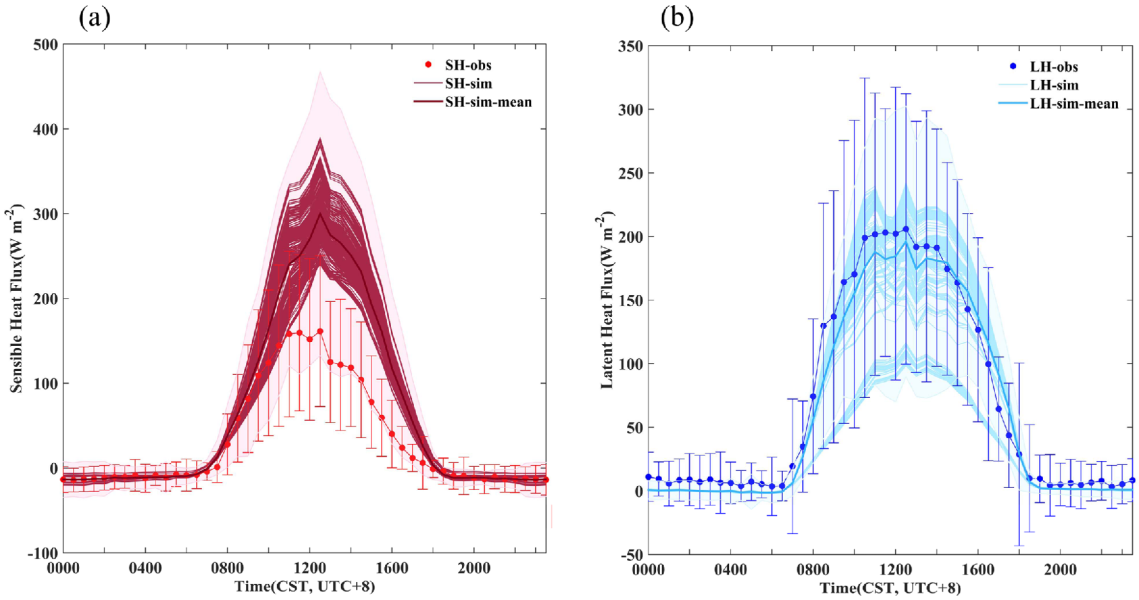

Fig. 14. Comparison of all the simulated values and observed values: (a) Sensible Heat Flux (W m^{-2}) and (b) Latent Heat Flux (W m^{-2}). The vertical bar is the standard deviation of the observed data and the shaded portion represents the standard deviation of simulated data.

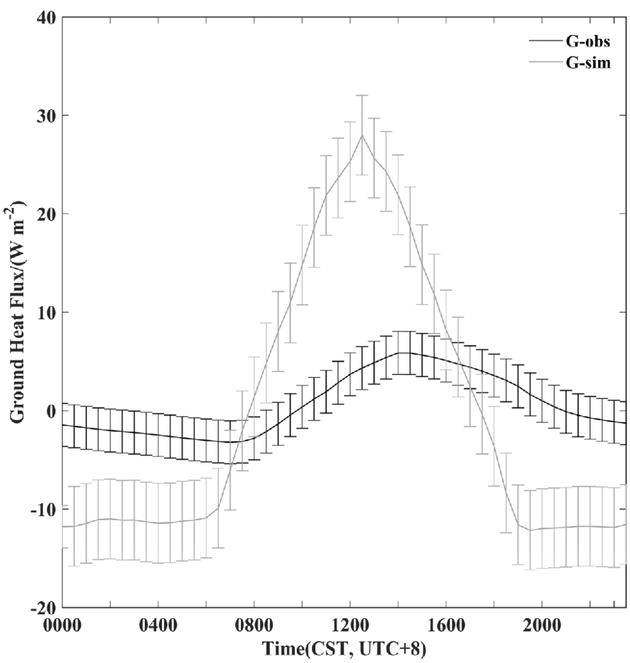

Fig. 15. Comparison of simulated values and observed values of Ground Heat Flux (W m^{-2}). The vertical bar is the standard deviation of the data.

vation means, so that SH + LH < Rn-G. However, when Noah-MP distributes energy, it first calculates the heat capacity and thermal conductivity of each part (e.g. vegetation canopy, soil layer, snow layer). Then the model begins to distribute the radiant energy, which first calculates the albedo of the surface and then calculates the net solar radiation flux on the surface. Finally, it solves the energy balance equation and then solves

Table 9. Statistical results of simulated values and observed values.

Evaluation Criteria	Ground Heat Flux
Mean (Observation)	0.583
Mean (Simulation)	−0.0943
Bias	−0.677
MRB	−0.693
MAE	11.0
MRE	−3.05
RMSE	13.8
Correlation coefficient	0.796

the energy flow in vegetation and bare ground. The energy expression in Noah-MP is Rn = La (net longwave radiation) + SH + LH + G, without considering the energy contained in the energy convection. The near-stratigraphic observation of turbulence energy is imbalanced and will be conducted through the near-surface turbulence parameterization scheme to the land surface process model. When the energy of the turbulent flux is lower than the available energy, the energy is imbalanced and the surface longwave radiation and the soil temperature simulated by the LSM are significantly larger. On the other hand, the built-in LAI values of this model are not the data of 2015, but the data of 2010, which is also one of the reasons for the bias. In addition, the simulations of G need to be analyzed as the simulation bias in G may affect the distribution of energy fluxes among the other components (Guo et al., 2002) in the model. The simulation of G is shown in Fig. 15. It can be seen that the gap between the simulated value and the observed value is large. The comparison results are shown in Table 9. The correlation coefficient between the

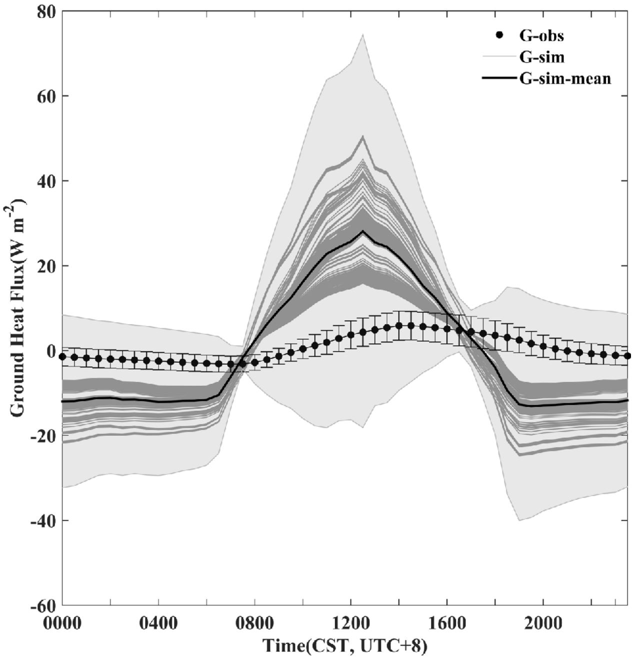

Fig. 16. Comparison of all the simulated values and observed values of Ground Heat Flux (W m^{-2}). The vertical bar is the standard deviation of the observed data and the shaded portion represents the standard deviation of simulated data.

observed and simulated values is as high as 0.796. However, the deviation is large, and the simulated mean is less than the observed mean.

In addition, all simulated values of G are compared with the observed values to determine the reason for the poor simulation of G in the model. As what shown in Fig. 16, the variation ranges of all the simulated values of G are significantly larger than the observed values. And the time, at which the peak appears, of the observed value is lagging behind the simulated values. Obviously, this is also due to the parameterization scheme of the model. This situation will eventually lead to the above simulation bias of LH and SH.

According to the description in section 3. b, R_c increases when LH increases, and decreases when SH increases. Therefore, the simulation bias of SH and LH in the Noah-MP will lead to the underestimation of R_c. Theoretically, the above situation should make the V_d overestimated, but the actual situation is the opposite, indicating that although Noah-MP simulation bias exists, there are other factors cause the underestimation of V_d.

The single-point model used in the study is coupled by Noah-MP and WDDM. Therefore, it is necessary to analyze the possible bias caused by WDDM. The Wesely (1989) scheme used in WDDM is a comprehensive dry deposition parameterization scheme developed on the basis of observations of the atmospheric dry deposition velocity. And Wesely (1989) scheme has been widely used in regional and global models (Wu et al., 2011). During the development of the model, the main observation was the dry deposition rate of SO_2 and O_3, with a very small amount of observation of NO_2 dry deposition velocity (Wesely and Hicks, 2000). The resistance parameters of other gaseous species should be modified on the base of the parameters of SO_2 and O_3. In the course of adjustment, the model will also produce biases. Wu et al. (2011) found that adjusting the parameters of the Wesley scheme to achieve parameter localization can effectively improve the V_d simulation results. So, Wesley scheme built-in parameter setting is not accurate, which is the main reason for the underestimation of V_d.

Based on the above results, it can be proved that single-point dry-deposition model coupled by Noah-MP and WDDM can effectively simulate the diurnal variation of V_d (NO_x), but the value of V_d (NO_x) is underestimated. In order to effectively improve the simulation result and reduce the bias, besides the adjustment of the combination of physical options, the future research work should focus on the improvement of the model parameterization. In addition, the research result of the simple single point dry deposition mechanism model can be extended to WRF-Chem and other complex "On-Line" air quality models, which can optimize the simulation results of the dry deposition velocity of nitrogen.

5. Conclusions

In this study, the Noah-MP land surface model and the dry deposition module in the WRF-Chem atmospheric chemistry model were coupled to form a dry deposition single-point model, and the model was driven by the micro-meteorological observation of the Dinghushan Forest Ecosystem Location Station. A series of numerical experiments were carried out to identify the key processes influencing the calculation of dry deposition velocity, and the effects of various surface physical and plant physiological processes on dry deposition were discussed. And the conclusions are as follows.

1) The observed V_d (NO_x) varies from 0.12 to 0.20 cm s^{-1}, with higher (lower) velocity observed in the daytime (nighttime). High values peaks at 0800 CST and 1900 CST, which are related to the emission and transportation of local pollutants, and the accumulation and release of pollutants in the boundary layer.

2) The single-point model is able to capture the observed V_d (NO_x) well with the optimal simulation ranges from 0.0075 to 0.10 cm s^{-1}. However, the model still significantly underestimates V_d (NO_x), which is related to that the model does not take into account the transport of peripheral contaminants, resulting in the obvious bias occur at dusk and morning.

3) The systematic bias caused by the parameterization scheme and the built-in parameters in the Wesely scheme are the main causes of $V_d(NO_x)$ underestimation. The Noah-MP calculation mechanism and built-in data error also have some influence on the results. Therefore, in order to effectively carry out the numerical simulation work for nitrogen deposition, we need to optimize the parameters at first. The results of simple single-point model can be extended to the "On-Line" model to

optimize the simulation of dry deposition of nitrogen.

In general, through the coupling of Noah-MP, a multi-layer canopy radiation and energy balance model with WDDM, this study identifies the main physical processes that need to be improved in the current model, and discusses the impact generated by main physical and physiological processes on dry deposition velocity simulation. So as to provide more effective research tools for the Dinghushan forest area where the nitrogen deposition is serious.

Acknowledgements. This work was supported by the National Key Research and Development Program of China (2017-YFC0210103, 2017YFC0210105), National Science Fund for Distinguished Young Scholars (41425020), the State Key Program of National Natural Science Foundation of China (91644215), National Natural Science Foundation of China (Grant No. 41705123), Guangdong Provincial scientific planning project (2016B050502005), the High-Performance Grid-computing Platform of Sun Yat-sen University, and we would like to thank the Dinghushan Forest Ecosystem Research Station of the Chinese Academy of Sciences for the data support.

Edited by: Yunsoo Choi

References

Ameur-Bouddabbous, I., J. Kasperek, A. Barbier, F. Harel, and B. Hannoyer, 2012: Transverse approach between real world concentrations of SO_2, NO_2, BTEX, aldehyde emissions and corrosion in the Grand Mare tunnel. *J. Environ. Sci.*, **24**, 1240-1250, doi:10.1016/S1001-0742(11)60936-4.

Aubinet, M., and Coauthors, 2000: Estimates of the annual net carbon and water exchange of forests: The euroflux methodology. *Adv. Ecol. Res.*, **30**, 113-175, doi:10.1016/S0065-2504(08)60018-5.

Ball, J. T., I. E. Woodrow, and J. A. Berry, 1987: A Model Predicting Stomatal Conductance and its Contribution to the Control of Photosynthesis under Different Environmental Conditions. In *Progress in Photosynthesis Research: Volume 4 Proceedings of the VIIth International Congress on Photosynthesis Providence*, J. Biggins Ed., Springer, 221-224, doi:10.1007/978-94-017-0519-6.

Berry, J. A., and J. K. Raison, 1981: Responses of macrophytes to temperature. In *Physiological Plant Ecology I*, O. L. Lange et al. Eds., Springer Berlin Heidelberg, 277-338.

Bi, X., and Coauthors, 2007: Seasonal and diurnal variations in moisture, heat, and co2 fluxes over grassland in the tropical monsoon region of southern China. *J. Geophys. Res.*, **112**, 185-194, doi:10.1029/2006-JD007889.

Brix, H., 1962: The effect of water stress on the rates of photosynthesis and respiration in tomato plants and loblolly pine seedlings. *Physiol. Plantarum*, **15**, 10-20.

Byun, D., and K. L. Schere, 2006: Review of the governing equations, computational algorithms, and other components of the models-3 community multiscale air quality (CMAQ) modeling system. *Appl. Mech. Rev.*, **59**, 51-77, doi:10.1115/1.2128636.

Canfield, D. E., A. N. Glazer, and P. G. Falkowski, 2010: The evolution and future of Earth's nitrogen cycle. *Science*, **330**, 192-196, doi:10.1126/science.1186120.

Chen, L., S. Peng, J. Liu, and Q. Hou, 2012: Dry deposition velocity of total suspended particles and meteorological influence in four locations in Guangzhou, China. *J. Environ. Sci.*, **24**, 632-639, doi:10.1016/S1001-0742(11)60805-X.

Chen, F., and Coauthors, 2014: Modeling seasonal snowpack evolution in the complex terrain and forested Colorado Headwaters region: A model intercomparison study. *J. Geophys. Res.*, **119**, 13795-13819, doi:10.1002/2014JD022167.

Collatz, G. J., J. T. Ball, C. Grivet, and J. A. Berry, 1991: Physiological and environmental regulation of stomatal conductance, photosynthesis and transpiration: a model that includes a laminar boundary layer. *Agric. Forest Meteor.*, **54**, 107-136.

Cui, J., J. Zhou, and H. Yang, 2010: Atmospheric inorganic nitrogen in dry deposition to a typical red soil agro-ecosystem in southeastern China. *J. Environ. Monitor.*, **12**, 1287-1294, doi:10.1039/b922042a.

Deng, J., T. J. Wang, S. Li, M. Xie, and J. L. Fan, 2009: Study on atmospheric nitrogen oxidant and deposition flux in suburban of Nanjing. *Sci. Meteorol. Sin.*, **29**, 25-30.

Dickinson, R. E., M. Shaikh, R. Bryant, and L. Graumlich, 1998: Interactive canopies for a climate model. *J. Climate*, **11**, 2823-2836, doi:10.1175/1520-0442(1998)011<2823:ICFACM> 2.0.CO;2.

Du, E., W. de Vries, J. N. Galloway, X. Hu, and J. Fang, 2014: Changes in wet nitrogen deposition in the united states between 1985 and 2012. *Environ. Res. Lett.*, **9**, 095004, doi:10.1088/1748-9326/9/9/095004.

Erisman, J. W., and G. Draaijers, 2003: Deposition to forests in Europe: Most important factors influencing dry deposition and models used for generalization. *Environ. Pollut.*, **124**, 379-388, doi:10.1016/S0269-7491(03)00049-6.

Fan, J.-L., Z.-Y. Hu, T. Wang, and J. Zhou, 2009: Dynamics of dry deposition velocities of atmospheric nitrogen compounds in a broadleaf forestland. *China Environ. Sci.*, **29**, 574-577.

Galloway, J. N., and E. B. Cowling, 2002: Reactive nitrogen and the world: 200 years of change. *AMBIO*, **31**, 64-71, doi:10.1579/0044-7447-31.2.64.

Gao, Z., G. T.-J. Chen, and Y. Hu, 2007: Impact of soil vertical water movement on the energy balance of different land surfaces. *Int. J. Biometeorol.*, **51**, 565-573, doi:10.1007/s00484-007-0095-6.

Gao, Y., K. Li, F. Chen, Y. Jiang, and C. Lu, 2015: Assessing and improving Noah-MP land model simulations for the central Tibetan Plateau. *J. Geophys Res.*, **120**, 9258-9278, doi:10.1002/2015JD023404.

Gruber, N., and J. N. Galloway, 2008: An Earth-system perspective of the global nitrogen cycle. *Nature*, **451**, 293-296, doi:10.1038/nature06592.

Guo, W., S. Sun, and Y. Qian, 2002: Case analyses and numerical simulation of soil thermal impacts on land surface energy budget based on an off-line land surface model. *Adv. Atmos. Sci.*, **19**, 500-512, doi:10.1007/s00376-002-0082-0.

Han, K. M., and C. H. Song, 2012: A budget analysis of NO_x column losses over the Korean peninsula. *Asia-Pac. J. Atmos. Sci.*, **48**, 55-65, doi:10.1007/s13143-012-0006-6.

Hole, L. R., S. H. Brunner, J. E. Hanssen, and L. Zhang, 2008: Low cost measurements of nitrogen and sulphur dry deposition velocities at a semi-alpine site: Gradient measurements and a comparison with deposition model estimates. *Environ. Pollut.*, **154**, 473-481, doi:10.1016/j.envpol.2007.06.061.

Horii, C. V., J. W. Munger, S. C. Wofsy, M. Zahniser, D. Nelson, and J. B. McManus, 2006: Atmospheric reactive nitrogen concentration and flux budgets at a Northeastern U.S. forest site. *Agric. Forest Meteorol.*, **133**, 210-225, doi:10.1016/j.agrformet.2006.03.005.

Horton, R., K. L. Bristow, G. J. Kluitenberg, and T. J. Sauer, 1996: Crop residue effects on surface radiation and energy balance - review. *Theor. Appl. Climatol.*, **54**, 27-37, doi:10.1007/BF00863556.

Jarvis, P. G., 1976: The interpretation of the variations in leaf water potential and stomatal conductance found in canopies in the field. *Philos. Trans. Roy. Soc. London*, **273**, 593-610.

Kong, G.-H., Z.-L. Huang, Q.-M. Zhang, S.-Z. Liu, J.-M. Mo, and D. Q. He, 1996: Type, structure, dynamics and management of the lower subtropical evergreen broad-leaved forest in the Dinghushan Biosphere Reserve of China. *Tropics*, **6**, 335-350, doi:10.3759/tropics.6.335.

Kumar, A., F. Chen, M. Barlage, M. B. Ek, and D. Niyogi, 2014: Assessing impacts of integrating modis vegetation data in the weather research and forecasting (WRF) model coupled to two different canopy-resistance approaches. *J. Appl. Meteor. Climatol.*, **53**, 1362-1380, doi:10.1175/JAMC-D-13-0247.1.

Lee, X., 1998: On micrometeorological observations of surface-air exchange over tall vegetation. *Agric. Forest Meteor.*, **91**, 39-49, doi:10.1016/S0168-1923(98)00071-9.

Li, Y.-X., Y.-S. Lou, and F.-C. Zhang, 2011: Comparison of stomatal conductance models for winter wheat. *Chinese J. Agrometeorol.*, **32**, 106-110, doi:10.3969/.jissn,1000-6362.2011.01.019 (in Chinese with English Abstract).

Li, Z., G. Yu, X. Wen, L. Zhang, C. Ren, and Y. Fu, 2005: Energy balance closure at ChinaFLUX sites. *Sci. China Ser. D.*, **48**, 51-62, doi:10.1360/05zd0005 (in Chinese with English Abstract).

Liu, H.-B., J.-J. Feng, and H.-M. Wang, 2005: The characteristic of the reverse temperature about low air in Jinan. *J. Shandong. Meteor.*, **25**, 27-28 (in Chinese with English Abstract).

Liu, X., and Coauthor, 2013: Enhanced nitrogen deposition over China. *Nature*, **494**, 459-462, doi:10.1038/nature11917.

Liu, Y. W., Xu-Ri, Y. S. Wang, Y. P. Pan, and S. L. Piao, 2015: Wet deposition of atmospheric inorganic nitrogen at five remote sites in the Tibetan plateau. *Atmos. Chem. Phys.*, **15**, 11683-11700, doi:10.5194/acp-15-11683-2015.

Lü, C., and H. Tian, 2007: Spatial and temporal patterns of nitrogen deposition in China: Synthesis of observational data. *J. Geophys. Res.*, **112**, 229-238, doi:10.1029/2006JD007990.

Mcrae, G. J., W. R. Goodin, and J. H. Seinfeld, 1982: Mathematical Modeling of Photochemical Air Pollution. EQL Report No. 18, 661 pp.

Niu, G.-Y., and Z.-L. Yang, 2004: Effects of vegetation canopy processes on snow surface energy and mass balances. *J. Geophys. Res.*, **109**, 2543-2552, doi:10.1029/2004JD004884.

______, ______, R. E. Dickinson, and L. E. Gulden, 2005: A simple TOPMODEL-based runoff parameterization (SIMTOP) for use in global climate models. *J. Geophys. Res.*, **110**, 3003-3013, doi:10.1029/2005JD006111.

______, ______, ______, ______, and H. Su, 2007: Development of a simple groundwater model for use in climate models and evaluation with Gravity Recovery and Climate Experiment data. *J. Geophys. Res.*, **112**, 277-287, doi:10.1029/2006JD007522.

______, and Coauthors, 2011: The community Noah land surface model with multi-parameterization options (Noah-MP): 1. Model description and evaluation with local-scale measurements. *J. Geophys. Res.*, **116**, 1248-1256, doi:10.1029/2010JD015139.

Niu, H. S., R. Xu, Z. C. Zhang, and Z. Z. Chen, 2005: A Jarvis stomatal conductance model under considering soil moisture condition. *Chinese J. Ecol.*, **24**, 1287-1290 (in Chinese with English Abstract).

Pan, Y. P., Y. S. Wang, G. Q. Tang, and D. Wu, 2012: Wet and dry deposition of atmospheric nitrogen at ten sites in northern China. *Atmos. Chem. Phys.*, **12**, 6515-6535, doi:10.5194/acpd-12-753-2012.

Petroff, A., A. Mailliat, M. Amielh, and F. Anselmet, 2008: Aerosol dry deposition on vegetative canopies. Part 1: Review of present knowledge. *Atmos. Environ.*, **42**, 3625-3653, doi:10.1016/j.atmosenv.2007.09.043.

Pilegaard, K., P. HummelshØj, and N. O. Jensen, 1998: Fluxes of ozone and nitrogen dioxide measured by eddy correlation over a harvested wheat field. *Atmos. Environ.*, **32**, 1167-1177, doi:10.1016/S1352-2310(97)00194-5.

Sharma, S. K., A. Datta, T. Saud, M. Saxena, T. K. Mandal, Y. N. Ahammed, and B. C. Arya, 2010: Seasonal variability of ambient NH_3, NO, NO_2 and SO_2 over Delhi. *J. Environ. Sci.*, **22**, 1023-1028, doi:10.1016/S1001-0742(09)60213-8.

Shen, J. L., A. H. Tang, X. J. Liu, A. Fangmeier, K. T. W. Goulding, and F. S. Zhang, 2009: High concentrations and dry deposition of reactive nitrogen species at two sites in the North China Plain. *J. Environ. Pollut.*, **157**, 3106-3113, doi:10.1016/j.envpol.2009.05.016.

Shen, J., L. Zhong, S. Ye, D. Chen, M. Jiang, M. Xie, L. Wen, Y. Zhang, and D. Yue, 2015: Air pollution characteristics in dry and wet seasons in the Pearl River Delta. *China Sci. paper*, **10**, 1748-1751 (in Chinese with English Abstract).

Shi, J. H., Z. H. Huang, X. Y. Zhou, C. Zhang, X. J. Ouyang, and L. Li, 2006: The regeneration strategies and spatial pattern of woody species in the mixed coniferous and broadleaf forest in Dinghu mountains. *J. Nanjing Forest. Univ.*, **30**, 34-38 (in Chinese with English Abstract).

Stevens, C. J., N. B. Dise, J. O. Mountford, and D. J. Gowing, 2004: Impact of nitrogen deposition on the species richness of grasslands. *Science*, **303**, 1876-1879, doi:10.1126/science.1094678.

Sun, C. L., and S. D. Xie, 2014: Study on critical loads of sulfur and nitrogen in the Pearl River Delta. *Chinese J. Environ. Sci.*, **35**, 1250-1255 (in Chinese with English Abstract).

Tang, X., G. Zhou, D. Wen, D. Zhang, and J. Yang, 2003: Distribution of carbon storage in a lower subtropical monsoon evergreen broad-leaved forest in Dinghushan Nature Reserve. *Acta Ecol. Sin.*, **23**, 90-99 (in Chinese with English Abstract).

Tariq, S., H. Zia, and H. Ali, 2016: Satellite and ground-based remote sensing of aerosols during intense haze event of October 2013 over Lahore, Pakistan. *Asia-Pac. J. Atmos. Sci.*, **52**, 25-33, doi:10.1007/s13143-015-0084-3.

Taub, D. R., J. R. Seemann, and J. S. Coleman, 2000: Growth in elevated CO_2, protects photosynthesis against high-temperature damage. *Plant. Cell. Environ.*, **23**, 649-656, doi:10.1046/j.1365-3040.2000.00574.x.

Turnipseed, A. A., and Coauthors, 2006: Eddy covariance fluxes of peroxyacetyl nitrates (PANs) and NO_y to a coniferous forest. *J. Geophys. Res.*, **111**, 1485-1493, doi:10.1029/2005JD006631.

Vaittinen, O., M. Metsälä, S. Persijn, M. Vainio, and L. Halonen, 2014: Adsorption of ammonia on treated stainless steel and polymer surfaces. *Appl. Phys.*, **115**, 185-196, doi:10.1007/s00340-013-5590-3.

Wang, C.-L., G.-Y. Zhou, X. Wang, C.-Y. Zhou, and G.-R. Yu, 2007: Energy balance analysis of the coniferous and broad-leaved mixed forest ecosystem in Dinghushan. *J. Trop. Meteorol.*, **23**, 643-651 (in Chinese with English Abstract).

Wang, X., S. Situ, W. Chen, J. Zheng, A. Guenther, Q. Fan, and M. Chang, 2016. Numerical model to quantify biogenic volatile organic compound emissions: The Pearl River Delta region as a case study. *J. Environ. Sci.*, **46**, 72-82, doi:10.1016/j.jes.2015.08.032.

Wesely, M. L., 1989: Parameterization of surface resistances to gaseous dry deposition in regional-scale numerical models. *Atmos. Environ.*, **23**, 1293-1304, doi:10.1016/0004-6981(89)90153-4.

______, and B. B. Hicks, 2000: A review of the current status of knowledge on dry deposition. *Atmos. Environ.*, **34**, 2261-2282, doi:10.1016/S1352-2310(99)00467-7.

Wu, Z., and Coauthors, 2011: Evaluating the calculated dry deposition velocities of reactive nitrogen oxides and ozone from two community models over a temperate deciduous forest. *Atmos. Environ.*, **45**, 2663-2674, doi:10.1016/j.atmosenv.2011.02.063.

Wu, Z. Y., L. Zhang, X. M. Wang, and J. W. Munger, 2015: A modified micrometeorological gradient method for estimating O3 dry deposition over a forest canopy. *Atmos. Chem. Phys.*, **15**, 7487-7496, doi:10.5194/acp-15-7487-2015.

Yang, R., and M. A. Friedl, 2003: Modeling the effects of three-dimensional vegetation structure on surface radiation and energy balance in boreal forests. *J. Geophys. Res.*, **108**, 1051-1062, doi:10.1029/2002JD003109.

Zhang, L., Y. Luo, G. Yu, and L. Zhang, 2010: Estimated carbon residence times in three forest ecosystems of eastern China: Applications of probabilistic inversion. *J. Geophys. Res.*, **115**, 137-147, doi:10.1029/2009JG001004.

Zhou, X.-Y., Z.-L. Huang, J.-H. Shi, X.-J. Ouyang, J. Li, and C. Zhang, 2004: Short-term dynamics of community composition and structure during succession of coniferous and broad-leaved mixed forest in Dinghushan. *J. Trop. Subtrop. Bot.*, **12**, 323-330 (in Chinese with English Abstract).

Zuo, J.-Q., J.-M. Wang, J.-P. Huang, W.-J. Li, G.-Y. Wang, and H.-L. Ren, 2010: Estimation of ground heat flux for a semi-arid grassland and its impact on the surface energy budget. *Plateau Meteor.*, **29**, 840-848 (in Chinese with English Abstract).